

Bistable Aerial Transformer (BAT): A Quadrotor Fixed-Wing Hybrid that Morphs Dynamically via Passive Soft Mechanism

Jessica Weakly*[†]

Department of Mechanical Engineering
University of Pennsylvania
Philadelphia, PA 19104 USA
Email: jmcw@seas.upenn.edu

Xuan Li[†]

Department of Mathematics
University of California, Los Angeles
Los Angeles, CA 90095 USA
email: xuanli1@math.ucla.edu

Tejas Agarwal

Department of Electrical Engineering
University of Pennsylvania
Philadelphia, PA 19104 USA
email: tejas.dce@gmail.com

Minchen Li

Department of Mathematics
University of California, Los Angeles
Los Angeles, CA 90095 USA
Computer Science Department
Carnegie Mellon University
Pittsburgh, PA 15213 USA
email: minchernl@gmail.com

Spencer Folk

Department of Mechanical Engineering
University of Pennsylvania,
Philadelphia, PA 19104 USA
email: sfolk@seas.upenn.edu

Chenfanfu Jiang

Department of Mathematics
University of California, Los Angeles
Los Angeles, CA 90095 USA
email: chenfanfu.jiang@gmail.com

Cynthia Sung

Department of Mechanical Engineering
University of Pennsylvania,
Philadelphia, PA 19104 USA
email: crsung@seas.upenn.edu

ABSTRACT

Aerial vehicle missions require navigating trade-offs during design, such as the range, speed, maneuverability, and size. Multi-modal aerial vehicles enable this trade-off to be negotiated during flight. This paper presents a Bistable Aerial Transformer (BAT) robot, a novel morphing hybrid aerial vehicle (HAV) that switches between quadrotor and fixed-wing modes via rapid acceleration and without any additional actuation beyond those required for normal flight. The design features a compliant bistable mechanism made of thermoplastic polyurethane (TPU) that bears a large mass at the center of the robot's body. When accelerating, inertial forces transition the vehicle between its stable modes, and a four-bar linkage connected to the bistable mechanism folds the vehicle's wings in and out. The paper includes the full robot design and a comparison of the fabricated system to the elastodynamic simulation. Successful transitions between the two modes in mid-flight, as well as sustained flight in each mode indicate that the vehicle experiences higher agility in the quadrotor mode and higher flight efficiency in the fixed-wing mode, at an energy equivalent cost of only 2 s of flight time per pair of transitions. The vehicle demonstrates how compliant and bistable mechanisms can be integrated into future aerial vehicles for controllable self-reconfiguration for tasks such as surveillance and sampling that require a combination of maneuverability and long-distance flight.

*Corresponding author. [†] equal contribution



Fig. 1: The fabricated BAT prototype with quadrotor (top) and fixed-wing (bottom) modes. Shown hovering during an outdoor flight test over the University of Pennsylvania's Franklin Field.

1 Introduction

Current advancements in unmanned aerial vehicles (UAVs) have shown them to be excellent platforms for sensing and monitoring. Small-scale UAVs ($<1\text{kg}$), in particular, have demonstrated high agility and autonomy in a variety of scenarios, leading to a large boom in commercialization and usage. However, while UAVs come in multiple forms, few exhibit the combination of range, endurance, maneuverability, and small size that are required for most missions (see [1; 2; 3] for review). While fixed-wing aircraft are capable of high efficiency and long-range flight, they cannot match the three-dimensional (3D) agility of their multicopter counterparts. Multicopters, on the other hand, can carry limited payloads (often dominated by the battery mass), and typically cannot last more than 10-20 minutes in laboratory settings. Thus aerial vehicle design requires a careful trade-off between aircraft weight, design complexity, flight stability, agility, and flight range.

Morphing offers a way to adjust the performance after deployment, allowing this trade-off to be negotiated mid-flight, rather than only at design time [4; 5]. For example, vehicles may change propeller layout to trade off stability with being able to fit through gaps [6; 7], tilt rotors for increased quadrotor efficiency [8; 9], modify wing geometry for enhanced maneuverability [10], or even incorporate non-flight locomotion modes [11; 12; 13]. Increasingly, morphing aerial vehicle designs have become focused on wing modification to optimize flight performance and address the challenge of limited battery life [14]. Aerial vehicles twist wings for efficient control [15], fold wings to reject gusts [16; 17], reduce wing area asymmetrically to exploit wind conditions [17], tilt wings [18] to switch from a hovering mode to a cruising mode, rotate wings to enter an efficient hover mode inspired by maple seeds [19], or sweep wings to trade off agility and efficiency [20]. However, existing morphing aerial designs often rely on precise configuration changes that incur added weight [11; 12], actuation [13; 7], and complex control [21; 13].

At the same time, compliance has emerged as a strategy for providing a robot with *mechanical intelligence*, that is, the ability to passively conform or adjust to task requirements that are unknown a priori [22]. In applications as varying as manipulation [23; 24], locomotion [24], navigation [25], and human-robot interaction [26], compliance has enabled robots to achieve desired behaviors while simplifying actuation, fabrication, and control, simply by tuning the mechanical properties of the structure. In aerial morphing, similar ideas have been demonstrated, for example by attaching springs to the arms of a quadrotor to allow it to fold to fit through windows or other tight spaces [27; 28] or transport payloads [28], by adding a compliant structure that allows rotors to tilt at high thrust to reduce system drag [29], or by incorporating an elastic element to enable a micro winged aircraft to control pitch using passive wing sweep changes controlled by thrust [30]. The compliance in these vehicles enhances their functionality without requiring additional actuators, although it imposes limits on the thrusts and motions that can be performed within each mode.

Bistable mechanisms may alleviate this issue by providing stable modes that resist environmental disturbances or control

fluctuations. Bistable mechanisms are compliant structures that produce rapid, accurate switching between two different equilibria. Since they are lightweight, fast, and repeatable, these mechanisms have been utilized in a diverse set of robotic systems, such as jumping robots [31; 32], Venus fly-trap robots with high-speed grasping [33; 34], rowing aquatic robots [35], and mechanically intelligent crawling robots [36]. In these applications, a trigger pushes the mechanism past its unstable equilibrium, causing the mechanism to “snap-through” to its other equilibrium and producing an impulse on the robot. This can increase the speed of slow actuators or amplify the actuation stroke. Bistability can also act as a sensor or mechanically embedded trigger for robotic grippers [37; 38], which can be useful for highly dynamic grasps or aerial perching [39]. Since each desired configuration is stable, robots do not need to continuously consume electrical energy to maintain the grasp of the object. In aerial robots, incorporating a bistable structure into the frame of a quadrotor enables perching with a reduced mass compared to having two separate subsystems [40]. Bistable mechanism designs are generally directly actuated to switch between equilibria via motors [41; 32; 42], shape-memory actuators [33; 35], pneumatics [34], or contact forces [38; 40; 43].

In certain scenarios, bistable mechanisms may be triggered using the system’s own dynamics. A morphing propeller uses the centripetal forces on a mass connected to a bistable origami structure to increase the blade length [44]. In [45], a manipulator used accelerations to modify the shape of the fingers by causing snap-through of bistable origami units, allowing for three different grasp modes. Transformation of the bistable vertex occurs when the kinetic energy of the facets above the vertex exceeds the transformation energy barrier of the vertex.

In this paper, we present the Bistable Aerial Transformer (BAT) robot (Fig. 1), a morphing aerial vehicle that uses inertial triggering of a bistable mechanism to transition between quadrotor and fixed-wing modes. In previous work, we demonstrated on a rotating boom [46] how a bistable mechanism could be triggered by quadrotor thrusts. Here, we expand on the vehicle design and show that it is possible to control inertial switching in mid-flight. Compared to the previous work, we present an updated design, demonstrations of flight in both quadrotor and fixed-wing modes, and experimental evaluation of agility and energy trade-offs. The main contributions of this paper include:

- the BAT (Bistable Aerial Transformer), a morphing aerial vehicle capable of inertially-driven dynamic mid-flight reconfiguration between a quadrotor mode and a fixed-wing flight mode via a bistable mechanism;
- control trajectories for reliable mid-flight switching between flight modes;
- a detailed characterization of the mechanical properties of the driving bistable structure, including an analysis of the effect of hysteresis;
- demonstration of stable flight in each mode; and
- a preliminary empirical analysis of the energy consumption for each flight mode of the vehicle.

To our knowledge, the BAT is the first working example of an inertially driven self-reconfiguring aerial robot. The BAT exhibits mechanical intelligence by rejecting small disturbances due to the environment and by leveraging its own mass to achieve state-switching when an aggressive trajectory is flown.

The remainder of the paper is structured as follows. Section 2 gives an overview of the system design and functionality. Section 3 discusses the physical hardware of the system. Section 4 discusses the design process for the bistable mechanism, as well as its verification through compression testing. Section 5 details the control of the system, and the dynamic simulation used to test and develop the transition maneuvers. Finally, Section 6 demonstrates experimental results through indoor and outdoor flight testing.

2 System Overview

The BAT is a semi-rigid quadrotor with deployable wings that fold to transition in and out of fixed-wing flight mode (Fig. 1). In order to achieve this mode transition passively and without additional actuators, and design of the vehicle requires knowledge about the transition maneuver.

For the physical hardware (Fig. 2a), the key enabling feature is a 3D printed compliant bistable mechanism that deforms between and stabilizes the quadrotor and fixed-wing modes. This mechanism is used in place of the rigid arms commonly found in quadrotors. The robot is designed such that thrust forces from the propellers are applied on the robot’s outer ring, while 38% of the vehicle total mass, including the electronics and the battery, is fixed to the center of the bistable mechanism. As a result, when the vehicle accelerates or decelerates, inertial forces on the central mass deform the bistable mechanism and cause the robot to transition. When the center of the bistable mechanism is beneath the ring, the vehicle is in the quadrotor mode and the wings are folded. This is beneficial because gravity will be acting to keep the bistable structure in this position as the quadrotor operates in a primarily upright orientation. When the center of the bistable mechanism is above the ring, the vehicle is in the fixed-wing mode. The fixed-wing mode operates in a primarily pitched forward orientation, so the mechanism is not strongly influenced by gravity. Additionally, moving the mass of the battery forward helps ensure that the center of mass of the vehicle is slightly in front of the center of pressure of the wings.

For the transition maneuver (Sec. 5.2), mode changes of the BAT rely on a precise sequence of acceleration, pitching, and deceleration, illustrated in Fig. 2b. To transition from the fixed-wing mode to the quadrotor mode (F-to-Q), the vehicle

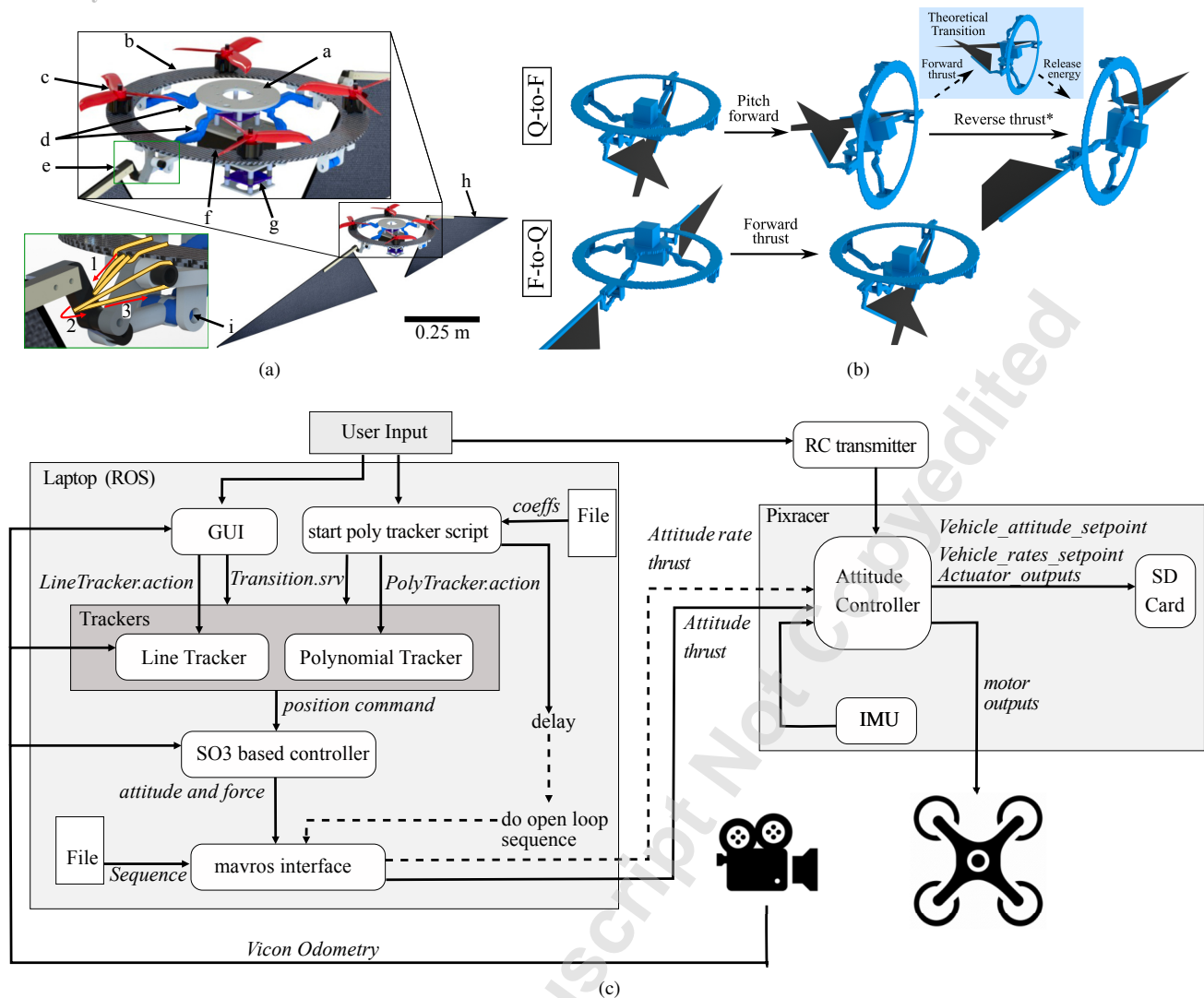


Fig. 2: (a) CAD model of the final design. The bistable mechanism (d, shown in blue), is designed via topology optimization and printed from thermoplastic polyurethane. The closeup of the wing linkage (e, boxed in green) also shows an elastic element that is added to counteract the weight of the wing. (b) State transition procedures. *A short forward thrust is used to stabilize the system orientation before the reverse thrust. (c) The control system diagram.

must accelerate rapidly, causing the central mass to lag behind the outer ring due to its inertia and the compliance of the bistable arms. As the bistable mechanism snaps through to its other equilibrium state, this motion is transmitted through a wing linkage that folds the wings in. To transition from the quadrotor mode to the fixed-wing mode (Q-to-F), the vehicle first pitches forward by about 90° , then also begins by accelerating rapidly, storing elastic energy in the bistable arms. Then, the vehicle rapidly decelerates, slowing down the outer ring relative to the central mass. Due to inertia, the central mass overshoots the outer ring and snaps the bistable mechanism into its other equilibrium state. Again, this motion is transmitted through the wing linkage that, in this case, folds the wings out. Simulations and videos of the mode transitions are shown in [Supplemental Materials Video 1](#).

3 Design of the Bistable Aerial Transformer

The BAT robot is based on an earlier prototype initially introduced in [46], and a detailed assembly of the prototype can be seen in Fig. 2a. In general, the robot's main body is a rigid 1/8"-thick carbon fiber ring (b) to which all other parts attach. A central housing laser cut from 1/8"-thick polyethylene terephthalate glycol (a) contains the Flycolor Raptor S-Tower 4-in-1 40A ESC board for controlling the motors and a 4S 15000 mAh 100C LiPo battery (f). Bistable thermoplastic polyurethane (TPU) arms (d) connect between the ring and the central housing at axles (i), which are 1" aluminum binding barrels mounted to 3D printed supports beneath the ring. Thus, the central housing is able to passively move in the direction

normal to the ring, depending on the motion of the robot. The bistable arms are also connected to a rigid four-bar linkage (e), laser cut from 1/4" acrylic, that folds and unfolds the flat triangular wings (h). The robot is equipped with four Dalprop T5045C propellers on ARRISX2206 2450kV motors (c) mounted to the rigid ring, which are each capable of providing 10 N of thrust. In contrast to typical quadrotor design, the Pixracer flight control board (g) that includes the IMUs and controls the attitude of the robot is mounted to the rigid ring rather than in the center of the vehicle. This ensures it is isolated from the vibrations and accelerations of the moving central housing, especially during snap-through.

The total mass of the prototype is 827 g, and the mass breakdown is shown in [Supplemental Materials Table 1](#). The flight time while hovering is 3.1 minutes¹, compared to 12 minutes of the ARRIS X220 racing drone on which the power system is based².

The new vehicle includes three main design features aimed at improving vehicle stability and control authority. First, the mechanical response of the bistable mechanism is designed to be asymmetric, making certain transitions easier when the vehicle pitches to align the gravitational forces with those required for transition. More details about this design can be found in Sec. 4. Second, the propellers are placed in an "X" configuration relative to the wing span. In this way, the wings and soft arms do not interfere with the wake of the propellers. Further, in fixed-wing mode, the vehicle has two propellers above the wings and two below, giving the vehicle better pitch authority and preventing motor burnout. This configuration allows the vehicle to use differential thrust to control the pitch in the fixed wing mode, similar to the quadrotor biplane tailsitter vehicle in [47]. Third, the wing was designed as a polyester fabric surface stretched between plastic beams, giving the robot a wingspan of 1.35 m. Each wing's triangular shape is formed by a span beam of 0.53 m and a beam at 110° offset that has a length of 0.23 m, giving it an approximate wing area of 0.057 m². When folded, the angle between the beams is 50°, leading to a wing area reduction of 18%. Since the weight of the wings was not accounted for in the bistable mechanism design, a rubber band is added to support the weight of the wings when extended in the hover orientation, as shown in the inset image in Fig. 2a. First the band is fastened around the carbon fiber ring (1), then the free end is brought under the wing output linkage (2) and looped over the joint fixed to the ring (3). The weight of the two wings is 77 g, while the linkages that rotate the wings weigh 30.8 g. [Supplemental Materials Sec. 1](#) provides additional fabrication details on the wing and wing linkage.

4 Bistable Mechanism

4.1 Design

The bistable mechanism is designed to be able to transition passively using only vehicle acceleration and to stabilize the mode against disturbances up to a certain magnitude. In order to achieve this behavior, the exact geometry was optimized via a topology optimization framework [48]. Building on [49], we optimize bistable arms by balancing two objectives: maximizing the difference of two switching forces (the forces required for snap-throughs between the two states), while minimizing the mean compliance under a force along the control path to guarantee sufficient structural stiffness. Additionally, the magnitude of the switching forces is limited. The complete optimization problem is formulated as:

$$\begin{aligned} \min_{\xi} \quad & n^T \left(\frac{\partial e(\rho, u^2)}{\partial u_i} - \frac{\partial e(\rho, u^1)}{\partial u_i} \right) + \alpha f^T u^3, \\ \text{s.t.} \quad & \begin{cases} u^1 = \operatorname{argmin}_u e(\rho, u), \quad \text{s.t. } u_i = \bar{u}_i^1, \\ u^2 = \operatorname{argmin}_u e(\rho, u), \quad \text{s.t. } u_i = \bar{u}_i^2, \\ u^3 = \operatorname{argmin}_u e(\rho, u) - u^T f, \\ n^T \frac{\partial e(\rho, u^1)}{\partial u_i} \leq f_1^*, \quad n^T \frac{\partial e(\rho, u^2)}{\partial u_i} \geq -f_2^*, \\ V(\rho) \leq \bar{V}. \end{cases} \end{aligned} \quad (1)$$

In this problem, the scalar α controls the weighting between two objectives mentioned above. The vector ξ is the set of design variables that controls the distribution of material, which is a vector of material density values on a set of evenly distributed particles in framework [48]. The vector n is the control path direction, i.e., the motion direction of central plate from the fixed-wing mode to the quadrotor mode. The function $e(\rho, u)$ is the density penalized total neo-Hookean hyperelasticity strain energy [50] for deformation modeling, which is given by

$$e(\rho, u) = \int_{\Omega} \rho^3 \Psi^E(F) dX, \quad (2)$$

¹The shorter flight time is because the ARRIS X220 racing drone weighs only 510 g and has the same battery. Additionally, the ring design used in this paper covers more of the propeller area than the standard X frame.

²<https://www.arrishobby.com/arris-x2206-2450kv-3-4s-brushless-motor-for-fpv-racing-drones-p0193.html>

$$\Psi^E(F) = \frac{\mu}{2}(F^T F - d) - \mu \log(\det F) + \frac{\lambda}{2} \log(\det F)^2, \quad (3)$$

where μ, λ are Lamé parameters, F is the deformation gradient, and $d = 2$ or 3 is the dimension of the problem. The vector f is a regularity force along n to increase the structural stiffness. For sensitivity analysis in each optimization iteration, we separately solve three displacement fields $\{u^1, u^2, u^3\}$, corresponding to three different static equilibria: $\{u^1, u^2\}$ are obtained by advancing the central port i of the structure by displacements \bar{u}_i^1, \bar{u}_i^2 to approximately reach the peak and the valley of the reaction force, respectively, and u^3 is obtained when the structure reaches equilibrium under the force f applied to port i . Further, these peak forces must lie between the target snap-through forces f_1^* and f_2^* to match practical needs. The volume constraint is used to avoid trivial design. The parameters used in our optimization are detailed in [Supplemental Materials Table 2](#).

We note that the optimization parameters f_1^* and f_2^* were chosen to create an asymmetric potential energy field for the bistable structure, such that it takes more energy to transform from F-to-Q than from Q-to-F. The F-to-Q transition is easier to execute since it can take place while the axis of the bistable mechanism's motion is aligned with gravity. In this orientation, the quadrotor mode is energetically favorable since there will be less gravitational potential energy in the central platform. So, we require that the structure be stiff enough to resist gravity in this direction, such that orientation alone cannot trigger accidental snap-through to quadrotor mode.

After the optimization converges, we obtain the structure inset in Fig. 3b with a predicted force-displacement curve shown as the grey dashed optimization curve. Note that applying an equal scaling on the force values and Young's modulus has no impact on the final design, as we only solve for static equilibria. Material parameter calibrations are performed after the design has been finalized, as discussed in Sec. 5. Additional design details can be found in [46], and simulations of the topology optimization process can be found in [Supplemental Materials Video 2](#).

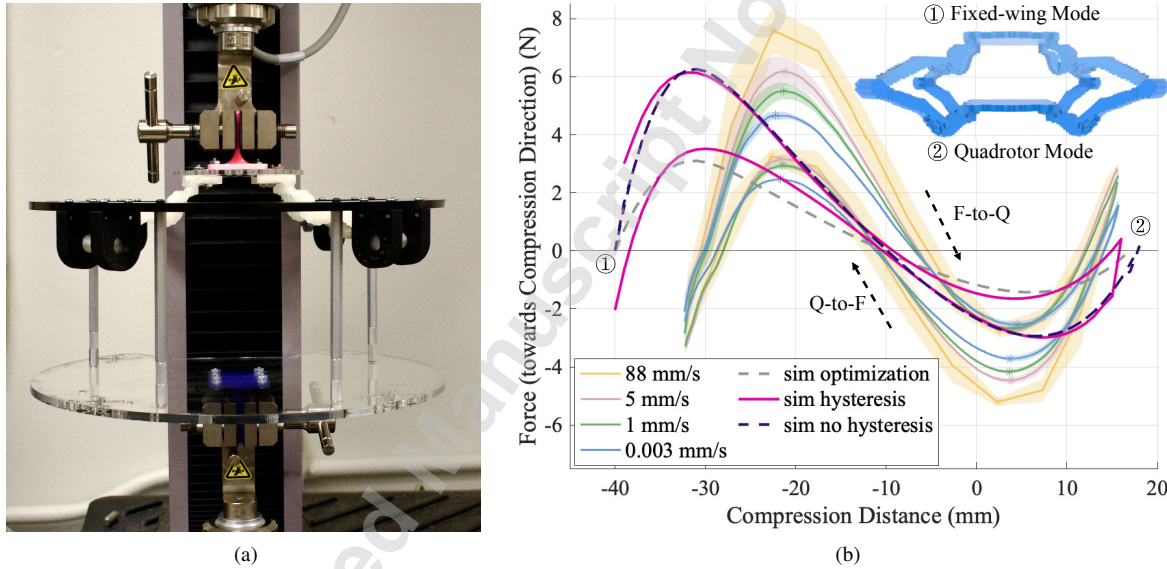


Fig. 3: (a) A photo of the compression testing setup on the MTS machine. (b) The MTS data for the optimized arms of the robot with simulated curves and final arm design overlaid. The simulated curve used in the optimization is shown, along with the calibrated curves with and without hysteresis that match the MTS data. Zero in the displacement corresponds to the location of the axes. Forces and displacements increase in the downward direction (towards quadrotor mode). The plot shows the mean with \pm standard deviation shaded for each tested speed, and the local extrema on each curve are indicated with a point. During flight, the speed is 88 mm/s on average. The test is repeated for slower speeds to determine the effect of the dynamics on the system. Each test includes 5 cycles at each speed, except 0.003 mm/s, which only includes 3 cycles.

4.2 Verification by Compression Testing

To verify the simulation and optimization of the mechanism itself, we conduct compression testing of the bistable mechanism on an MTS Criterion 41 with a 1 kN load cell. The bistable mechanism is 3D printed from thermoplastic polyurethane (TPU) on a MakerBot Replicator 2 printer. The estimated Young's modulus is about 10^7 Pa, which was determined empirically through MTS tests of a solid block of 3D printed TPU.

As shown in Fig. 3a, the ring is rigidly attached to the bottom tensile grip using a custom fixture, while the top of the central housing is attached to the top tensile grip. The zero for the crosshead is set to the first equilibrium, which is measured to be 32.3 mm above the axle location. Since it is possible the displacement range of the printed device will be different than predicted, we perform an initial compression and determine that a compression of 48 mm from the first equilibrium will cause the system to deform far enough to cross the second equilibrium. All the data is collected with a compression distance of 48 mm. In this setup, compression corresponds to the F-to-Q transition, while extension corresponds to the Q-to-F, as seen in Fig. 3b. To check the effect of viscoelasticity of the printed material, the test is conducted at four speeds: 0.003mm/s, 1mm/s, 5mm/s, and 88mm/s. Five cycles are conducted for each speed except for the slowest speed of 0.003mm/s, for which only three cycles are conducted since each cycle took over eight hours to complete and the variation between compressions is hypothesized to be low at small speeds.

The means and standard deviations at each speed are shown in Fig. 3b. The curves show that the physical system is bistable in each direction as designed. The standard deviation is small enough to prevent overlap between the curves throughout most of the motion, indicating consistent behavior of the system. The standard deviation also tends to be smallest as the curve is crossing the x-axis, meaning that the locations of the stable and unstable equilibria are consistent. Further, the locations of the extrema vary with speed by a maximum of only 2.2 mm, indicating that the overall shape of the curve remains similar.

Compared to the simulated behavior of the mechanism, the physical mechanism exhibits the asymmetric snap-through behavior as intended, with the Q-to-F direction requiring less force to snap-through. The unstable equilibrium location also matches that of the simulation. However, the physical mechanism exhibits significant viscoelasticity and hysteresis. Even in the quasi-static approximation using the 0.003 mm/s speed, the fabricated structure is stiffer than predicted. Additionally, the distance between the two equilibria is only about 43 mm, making them 25% closer together than the predicted stable equilibria. This discrepancy is attributed to the plastic deformation at a thin region of the arms which has measurably affected the location of the first equilibria by 8 mm. It is likely that the deformation at this joint has similarly affected the location of the second equilibria.

The MTS data shows that actuation of the bistable structure using motor thrusts will require more energy than initially predicted by the simulation due to the higher stiffness of the mechanism. To ensure that the BAT will still be able to execute mode transitions, we use these measurements to simulate the vehicle in Sec. 5 (using calibrated simulation curves shown in Fig. 3b). The effect of increased stiffness is moderated by the central platform's ability to tilt on the deployed system and in the dynamic simulation. When actuating by hand or on a boom, we observe that the central platform will always tilt as snap-through occurs unless it is directly constrained, indicating that tilting requires less energy and has a lower effective stiffness (Supplemental Materials Video 4). The motion of the equilibria due to plastic deformation may also lower the barrier to transition by reducing the effective distance to snap-through. However, this also means that while the robot will still be stable in each state, the wing deployment mechanism will not go through the entirety of its designed sweep angle.

5 Control and Dynamic Simulation

5.1 System Architecture

The robot's onboard flight controller is a Pixracer mounted to the rigid ring of the robot. The Pixracer runs a customized³ version of the PX4 autopilot firmware to handle the low-level attitude control, monitor the power consumption of the motors, and record flight data to an SD card. The control system architecture is diagrammed in Fig. 2c, and additional details regarding the architecture and functionality are included in Supplemental Materials Sec. 2. The Pixracer is equipped with inertial measurement units (IMUs) that it uses as feedback to the onboard attitude controller. The Pixracer receives attitude setpoints, which consist of collective thrust as well as the desired orientation quaternion of the robot and/or the desired angular rates (roll, pitch, yaw). During outdoor tests, the attitude setpoints are determined by the joysticks of the Spektrum DX6i radio transmitter; during indoor tests, attitude setpoints are sent from the Ground Control Station (GCS) and received via an ESP8266 wifi module. To achieve the attitude setpoint, the Pixracer computes and transmits commands for the ESC's connected to the motors.

During indoor tests, the GCS is a laptop running ROS. It is connected to both the vehicle and a Vicon motion capture system on separate wifi networks. The Vicon system tracks the ring and the central platform as two separate rigid bodies, but only the ring's odometry is used for control. A trajectory tracker computes desired positions at each time step to drive the robot along a given trajectory. The tracker sends position commands to the high-level SO3-based controller⁴ that takes in state information from the Vicon system and a position command and computes an attitude setpoint to be transmitted using MAVLink protocol. The propeller thrust coefficient is used in the computation of the attitude setpoint (Supplemental Materials Fig. 2).

We use two different trajectory tracking methods to generate position commands for the SO3-based controller: a min-

³minor change made to allow reverse thrust setpoints to be sent to the robot during offboard mode

⁴https://github.com/KumarRobotics/kr_mav_control

imum jerk line tracker and a piece-wise polynomial tracker. The difference between the polynomial tracker and the line tracker are two-fold: 1) the polynomial tracker allows the specification of multi-segmented polynomials for easy modification of the speed throughout the trajectory, and 2) this polynomial tracker does not depend on the robot's current position, meaning that it will provide the same commands to the robot each time it is executed. Note that there is still position feedback in the SO3-based controller that receives the position commands from both trajectory trackers.

5.2 Control

Control of the mode transition consists of two parts: the open-loop transition maneuver and the base trajectory. Before the mode transition begins, the line tracker is used to navigate the robot to the start location for the transition. The mode transition begins with a call for the polynomial tracker to start tracking the base trajectory; let the time the polynomial tracker begins be $t = 0$. The open-loop transition commands will begin to execute at $t = t_c$, where t_c is a predefined trigger time for the sequence.

The open-loop transition maneuver is a sequence of time durations t (s), pitch rates $\dot{\theta}$ (rad/s), and collective thrusts f_{ext} (% of full thrust) that generate attitude commands that are sent to the robot to cause snap-through of the bistable mechanism. The transition maneuver may contain an arbitrary number of segments. During the transition maneuver, the attitude setpoints computed by the SO3-based controller are overridden by the attitude setpoints specified by the sequence. The sequence is sent directly to the robot's onboard attitude controller in a time based manner, without any feedback on robot position. A flag in the attitude controller is set so that the robot directly uses the angular rates, rather than orientation setpoints, during the maneuver. This is used to produce the non-smooth commands for the rapid acceleration and deceleration needed for mode switching via the bistable mechanism.

The base trajectory Z^* is a polynomial that is tracked during the transition maneuver. Since the polynomial tracker is solely time-based and not dependent on position, it will continue to command the robot along the trajectory even if parts of the desired control are overridden by the open-loop sequence. Once the final setpoint of the base trajectory is reached, the robot is automatically commanded to hover at its current location. We defined trigger time t_c such that it shifts the timing of the open-loop control along the base trajectory. Thus, the base trajectory may function as either an approach or a recovery trajectory. In practice, the base trajectory acts as an approach trajectory for the Q-to-F transitions, giving the robot an initial velocity. For the F-to-Q transitions, the base trajectory functions as a recovery trajectory, allowing the robot to continue motion and reach a desired position setpoint.

5.3 Simulation and Calibration

In order to verify the robot design and select appropriate parameters for the transition maneuver, we simulated the robot using implicit MPM [51]. In particular, for each time step, we perform backward Euler time integration (taking time step size Δt) with semi-implicit Rayleigh damping. The resulting nonlinear system of equations can be reformulated into a minimization problem [52; 53]. Considering the assembly constraints, we solve

$$\begin{aligned} \min_{\Delta x} \quad & \frac{1}{2} \|\Delta x - \widetilde{\Delta x}\|_M^2 + \frac{1}{2\Delta t} \|\Delta x\|_{C^n}^2 + \Delta t^2 (e(x^n + \Delta x) - \Delta x^T f_{ext}^n) \\ \text{s.t.} \quad & Hu = 0, \end{aligned} \quad (4)$$

followed by a state update from the previous time step to the current time step:

$$v^{n+1} = \frac{\Delta x}{\Delta t}, \quad x^{n+1} = x^n + \Delta x, \quad (5)$$

where M is the mass matrix (including the battery, electronics, arms, wings and the rigid ring), e is the total strain energy, $C^n = \alpha M + \beta \frac{\partial^2 e}{\partial x^2}(x^n)$ is the damping matrix on bistable arms with α, β being damping coefficients, f_{ext}^n is the external force (motor thrusts), $v^{n,n+1}$ and $x^{n,n+1}$ denote velocities and positions from the known previous (n) and the unknown current ($n+1$) time steps, $\Delta x = v^n \Delta t + g \Delta t^2$, and $\|x\|_A^2$ represents $x^T A x$. The equation $Hu = 0$ represents the constraints that link different parts, where we ensure that parts on the same joint axle share the same displacement. This equality-constrained optimization is solved using the augmented Lagrangian method [54]. The damping coefficients used in simulation are $\alpha = 1e-5, \beta = 1e-7$.

To model hysteresis in the arm, we propose a model inspired by the viscoelasticity model in [55]. The strain energy in Equation 4 is appended with an extra term to account for hysteresis:

$$e(x) = \sum_q (\Psi^E(F_q) + \Psi^H(F_q[F_q^{V,n}]^{-1})) V_q, \quad (6)$$

with a new strain energy density for hysteresis:

$$\Psi^H(F) = \sum_{i=1}^d \Psi_i(\sigma_i). \quad (7)$$

Here, $\{\sigma_i\}_{i=1}^d$ is the singular values of F , and

$$\Psi_i(\sigma_i) = \begin{cases} 2\mu^H \epsilon_m (\log(\sigma_i) - \frac{\epsilon_m}{A}) + \frac{\mu^H}{A} \epsilon_m^2, & \log(\sigma_i) > \frac{\epsilon_m}{A}, \\ -2\mu^H \epsilon_m (\log(\sigma_i) + \frac{\epsilon_m}{A}) + \frac{\mu^H}{A} \epsilon_m^2, & \log(\sigma_i) < -\frac{\epsilon_m}{A}, \\ \mu^H A (\log(\sigma_i))^2, & \text{Otherwise} \end{cases} \quad (8)$$

where μ^H , ϵ_m , and A are parameters to control hysteresis. At the end of each time step, F^V is updated by the relation

$$F^{n+1} = Z(F^{n+1} [F^{V,n}]^{-1}) F^{V,n+1}, \quad (9)$$

where F^{n+1} is the deformation gradient at the force equilibrium, and Z is a projection map defined by

$$Z(F) = U \exp(A \log(\Sigma)) V^T, \quad F = U \Sigma V^T. \quad (10)$$

The interpretation of this model can be revealed by its strain-stress relation. Each component of the principal stress (τ_i^H) related to this energy is

$$\tau_i^H = \frac{\partial \Psi^H}{\partial \sigma_i} \sigma_i = \begin{cases} 2\mu^H \epsilon_m, & \log(\sigma_i) > \frac{\epsilon_m}{A}, \\ -2\mu^H \epsilon_m, & \log(\sigma_i) < -\frac{\epsilon_m}{A}, \\ 2\mu^H A \log(\sigma_i), & \text{Otherwise.} \end{cases} \quad (11)$$

The stress (τ_i^H) is a clamped linear function w.r.t. the strain ($\log \sigma_i$) by $\pm 2\mu^H \epsilon_m$ so that the amount of hysteresis is limited. The parameter A controls the sensitivity of hysteresis stress w.r.t. strain. As ϵ_m approaches zero, while keeping $\mu^H \epsilon_m$ fixed, the hysteresis will become rate-independent, which is only determined by whether the material is being expanded or compressed along each principal stretch direction.

Parameter Calibration The physical parameters of the simulation system are calibrated manually to match the MTS data (Fig. 3) qualitatively. The parameters are $E_{\text{arm}} = 10^7$ Pa, $\mu^H = 1.54 \times 10^8$ Pa, $A = 0.2$, $\epsilon_m = 10^{-4}$. We also run a simulation without hysteresis for Q-to-F transition to verify the necessity of reverse thrusts. To make it a fair comparison, we use $\hat{E}_{\text{arm}} = 1.3 \times 10^7$ Pa in this case, so that the range of the force curve stays roughly the same. The plots of reaction forces with respect to the displacements of the central platform simulated with and without hysteresis are shown in Fig. 3b.

With the calibrated physical hysteresis parameters, we test the BAT within our elastodynamic simulation framework. For the simulations of the F-to-Q transition maneuver, the robot is constrained to move along the direction of gravity. A forward thrust ($t = 0.15$ s, $f_{\text{ext}} = 90\%$) is applied. For the Q-to-F transition, the robot moves along the line perpendicular to gravity. Details of the thrust data will be provided in the next paragraph. We see that the bistable mechanism snaps through with this trajectory, as shown in Fig. 4c.

Necessity of Reverse Thrusts Theoretically, a large-enough forward thrust can store enough elastic energy in the arms to trigger the Q-to-F transition. However, due to the hysteresis, we find the theoretical transition from [46] difficult to achieve in the real BAT prototype. As seen in Fig. 4a, with a forward thrust ($t = 0.6$ s, $f_{\text{ext}} = 95\%$) on each motor, the Q-to-F transition is only triggered in the absence of hysteresis. Part of the reason is that the hysteresis adds damping to the system: the strain energy plot (Fig. 4b) generated by the simulation with hysteresis has fewer oscillations than the one generated by the simulation without hysteresis. This comparison experiment may be seen side by side in [Supplemental Materials Video 5](#). We then simulate the Q-to-F maneuver that consists of a forward thrust, followed by a reverse thrust ($t = [0.05, 0.15]$ s, $f_{\text{ext}} = [90, -95]\%$). Thrust stand tests show that the reverse thrust is only 50% of the corresponding forward thrust force ([Supplemental Materials Fig. 2](#)). This trajectory successfully triggers the snap-through, as seen in Fig. 4c.

6 Experimental Results

In order to evaluate the performance of the BAT, we conduct a series of indoor and outdoor flight tests. Indoor tests focus on demonstrating the transition maneuvers between quadrotor and fixed-wing flight modes, while outdoor tests aim to provide a preliminary characterization of the stability, agility, and energy consumption of each flight mode.

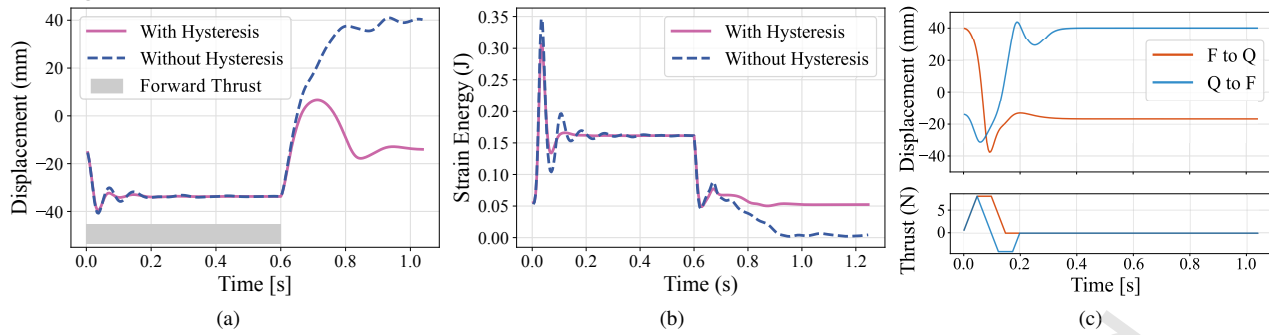
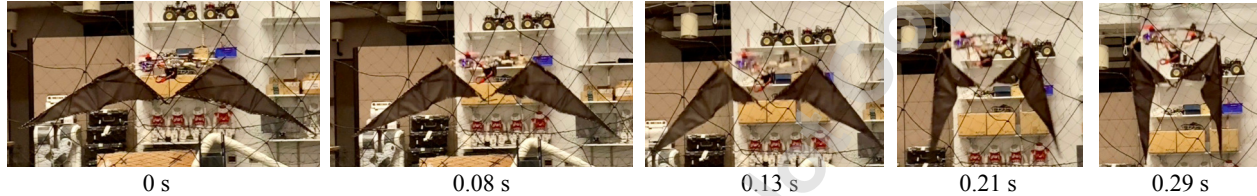


Fig. 4: We verify the BAT within our elastodynamic simulation framework. In plots (a) and (c), the displacement refers to the motion of the bistable mechanism, with 40 mm corresponding to fixed-wing mode and -15 mm corresponding to quadrotor mode. (a) The Q-to-F transition is only triggered in the absence of hysteresis. (b) The strain energy plots show that the hysteresis adds dampings to the system. (c) The displacement plot shows that when reverse thrust is used, the transitions are successfully triggered. Per-motor thrust values are also plotted.

Fixed-wing to Quadrotor



Quadrotor to Fixed-wing

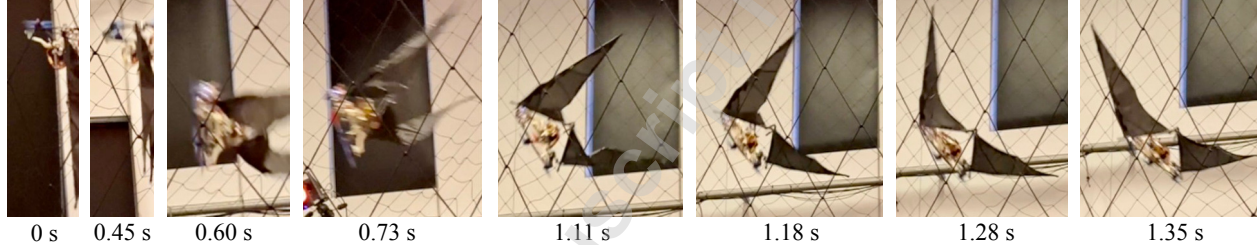


Fig. 5: Snapshots from [Supplemental Materials Video 6](#) of the mode transitions. [Top] F-to-Q: The BAT begins in fixed-wing mode and applies a large thrust. Around 0.13 seconds, the bistable mechanism has snapped-through to the other equilibrium, causing the wings to fold. [Bottom] Q-to-F: the BAT begins hovering in quadrotor mode, executes a vertical trajectory, pitches forward to 90°, and reverses the direction of thrust. Snap-through and wing deployment occurs, with a side effect of inducing a forward pitch.

6.1 Indoor Flight Tests

We demonstrate that the vehicle is able to successfully transition during flight by conducting tests inside an indoor test space equipped with an aerial net and a Vicon motion tracking system. For each mode transition, the BAT begins in hover mode at a specified starting location, then proceeds to execute the base trajectory and the open-loop maneuver (Sec. 5.2). We repeat each transition three times. The maneuvers may be viewed in [Supplemental Materials Video 6](#), and snapshots from the videos are shown in Fig. 5.

To verify that transitions occur, we track the position of the central platform relative to the ring, which corresponds to the displacement of the bistable mechanism. We place five 14 mm hemispherical reflective markers on the ring of the robot for Vicon feedback to the control loop and five on the central platform for tracking the bistable mechanism state.

6.1.1 Fixed-wing to quadrotor

For F-to-Q transition, snap-through only requires a large acceleration while the vehicle is in the quadrotor hover orientation. Starting from hover in fixed-wing mode, the following transition maneuver parameters were used: $t = 0.15$ s, $\dot{\theta} = 0$ rad/s, and $f_{ext} = 90\%$. The open-loop transition maneuver is executed at the start of the trajectory ($t_c = 0$). This sequence causes the BAT to immediately begin to snap-through into the quadrotor mode (Fig. 6a). To allow for a smooth

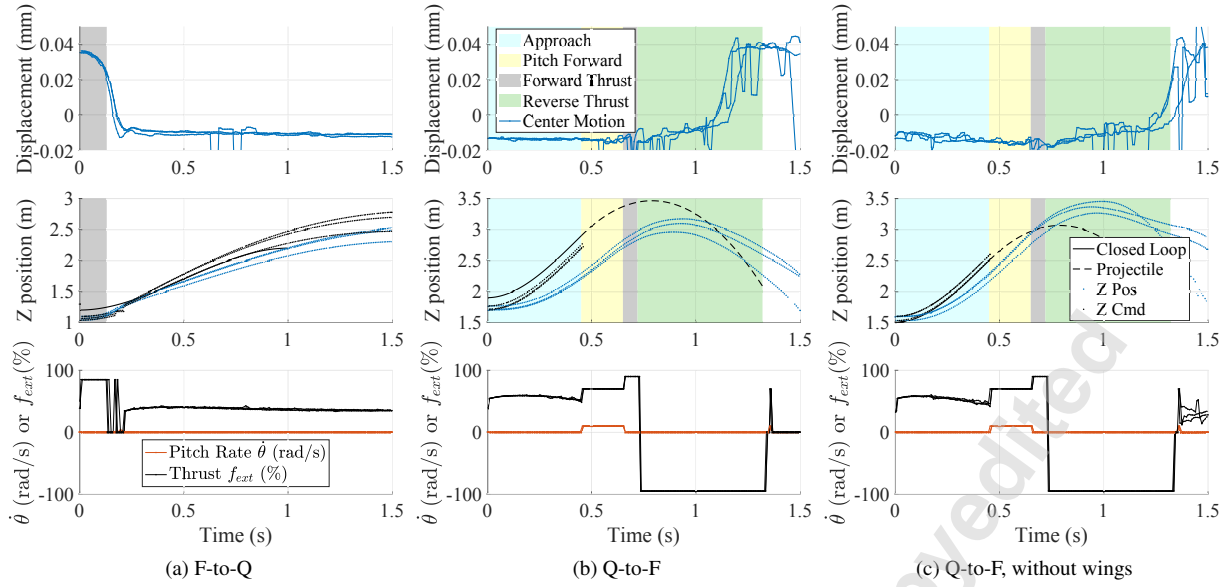


Fig. 6: Experimental Data from the Flight Tests. Top plots show the motion of the bistable mechanism and the control inputs, indicated by shaded regions, middle plots show the predicted, commanded, and actual position of the robot z coordinate during the transitions, and bottom plots show the actual pitch rate and thrust commands sent to the robot during the trials. (a) For F-to-Q, the displacement plot shows snap-through, and the robot z coordinate shows that the robot continues flying after snap-through. (b) For visual clarity, light smoothing is applied to the bistable mechanism displacement for Q-to-F (a moving median filter with a window of width three) due to orientation errors from marker occlusion. With the wings attached, the controller is not able to track the approach trajectory very well due to drag, preventing the robot from reaching the desired apex. (c) For Q-to-F without the wings, the snap-through takes longer. When the wings are not attached the robot tracks the commanded trajectory with a lag. The two trials with shallower end behavior were able to hover after snap-through.

recovery and show that the robot is stable in the quadrotor flight mode, we define $Z_{FtoQ}^* = -2t^3 + 3t^2$ to be a cubic base trajectory that causes the robot to rise in the z direction by 1 m over a period of 1 s.

After the open-loop segment, the closed-loop tracking continues for the remaining 0.85 seconds of the base trajectory duration and the robot maintains an upward trajectory, demonstrating stable flight in the quadrotor mode, as seen in Fig. 6a.

6.1.2 Quadrotor to fixed-wing

For the Q-to-F transition, the BAT first flies an approach base trajectory, then executes the open-loop transition maneuver. The open-loop commands for the quadrotor to fixed-wing transition are designed such that the robot pitches forward 90° , stabilizes its angular velocity, and then executes reverse thrust long enough for the transition to occur, as shown in Fig. 6b. The parameters are $t = [0.2, 0.07, 0.6]$ s, $\dot{\theta} = [10, 0, 0]$ rad/s, and $f_{ext} = [70, 90, -95]\%$.

The approach base trajectory is used to give the vehicle an initial velocity before beginning the open-loop transition maneuver to minimize the vertical space needed. Pitching forward to 90° and stabilizing makes the transition easier because gravity no longer opposes the switching of the bistable mechanism. However, a 90° pitch puts the robot in free-fall during the maneuver since the thrust vector does not have a vertical component.

We design the approach base trajectory by taking into account the vertical constraints of the test space and the duration of the open-loop sequence. The initial z coordinate of the robot $z_0 = 1.5$ m, is such that the robot does not touch the bottom of the netted test space. We assume a 1 m distance for the robot to accelerate prior to starting the transition maneuver. We find the initial velocity that minimizes the velocity at the end of the maneuver while keeping the robot's projectile motion under $z \leq 3.1$ m (a height of 3.5 m is allowable, but due to uncertainty in the robot's orientation and location during the open-loop trajectory, we use 3.1 m as a safety measure). Therefore, we define the base trajectory $Z_{QtoF}^* = -5.487t^3 + 7.407t^2$ to be a cubic spline in z where the distance of the trajectory would be 2 m and the duration of the trajectory is 0.9 s, but we set $t_c = 0.45$ s so that only the first half of the trajectory executes. This gives the robot an initial velocity of $v_0 = 3.33$ m/s when it starts the open-loop maneuver. The predicted location of the BAT's ring in z throughout the trajectory is shown in Fig. 6c. Note that with wings, the start height was raised to $z_0 = 1.9$ m such that the wings would not touch the bottom of the test space, which has some local high points that were not initially accounted for. Due to drag on the wings, the robot still does not exceed the maximum allowable height of 3.5 m with this trajectory in any of the trials.

6.1.3 Discussion

Snap-through occurs in all three trials for both F-to-Q and Q-to-F, indicating reliability of both transition maneuvers. This is determined by seeing that in each of the bistable mechanisms displacement plots in Fig. 6, the mechanism transitions from one equilibrium to the other. We corroborate our findings for the Q-to-F transitions with 120 fps videos taken from two different angles, since the high pitch angle of the robot and occlusion of markers on the central platform reduces the accuracy of the Vicon tracking. The videos confirm that snap-through behavior is seen in each trial.

The bistable mechanism displacement also shows that the snap-through behavior is consistent across transition trials. The lines in Fig. 6 being close together demonstrates qualitative consistency. The standard deviation of the time to snap-through for each transition is used to measure the consistency quantitatively. For F-to-Q, the times to reach the second equilibrium are 0.19 s, 0.21 s, and 0.23 s, determined by selecting the point on each curve that is the local minima before the displacement changes direction. The mean time for snap-through is 0.21 s and the standard deviation is only 0.02 s, which is the equivalent of two time steps for our high level controller. For Q-to-F, the bistable mechanism reached the fixed-wing equilibrium at 0.44 s, 0.47 s, and 0.53 s after the reverse thrust is applied. The mean time to snap-through after starting reverse thrust is 0.48 s with a standard deviation of 0.046 s. Noise in the data obscures the exact moment that central platform movement begins. There is a region where it moves slowly followed by a region where it moves more rapidly. The rapid motion has a duration of 0.10 s, 0.14 s, and 0.24 s across the three trials, for a mean of 0.16 s and a standard deviation of 0.072.

The standard deviation of the Q-to-F transition rapid motion region is 3.6 times larger than for the fixed-wing rapid motion region. This makes intuitive sense because there is error accumulation in the preceding open-loop segment. In Q-to-F, the snap-through does not start until midway through the open-loop maneuver, but it begins near the beginning of the F-to-Q maneuver.

The duration of rapid motion for Q-to-F is also shorter than that of F-to-Q, which makes sense because a portion of the motion for Q-to-F occurs in a gradual manner beforehand, as seen in Fig. 5 and [Supplemental Materials Video 6](#). From Fig. 6, we also see that the addition of wings reduces the amount of reverse thrust needed for snap-through to occur, as indicated by the mode switch occurring sooner. This is due to angular momentum in the wings and the inclusion of the rubber band. The inertia of the wings will help it complete snap-through once they start rotating. While the rubber band is necessary to support the mass of the wing during an upright orientation, it also aids the transition in the forward flight orientation.

Compared to simulation, the snap-through in real-world experiments occurs at a slower rate, with snap-through taking two times longer for F-to-Q than predicted. This discrepancy is attributed to the idealized assumption of friction-free joints in the simulation environment as well as drag on the wings.

The plots in Fig. 6, show that there is tracking error in the z direction, particularly for the Q-to-F cases. The main reason for this is that the polynomial being tracked with the polynomial tracker is not quite feasible. This is due in part to it being a cubic spline, rather than a minimum snap-trajectory, but could also be affected by a time delay in the control or the aggressiveness of the trajectory. In the case without wings, the robot first undershoots the desired trajectory and then overshoots. This is because during the open-loop maneuver, pitch forward does not happen instantaneously. During those 0.2 s, the robot is still providing a large collective thrust with a component in the z direction, hence a steeper slope in the actual motion than in the dashed projectile motion curve. However, for the case with wings, there is consistent undershooting, due to the drag on the wings that prevents the robot from reaching the designed initial velocity.

The higher apex of projectile motion in the case without wings ([Supplemental Materials Video 7](#)) allowed for recovery into a hovering position of the Q-to-F maneuver in two out of three trials, but the limited space prevents recovery with wings. One of the challenges with recovery is that the robot finishes the open-loop segment pitched past 90° (discussed further in next paragraph). When the wings are detached, the two trials with higher Z value at the time of 1.5 s were able to recover into the hover orientation and stop the projectile motion (Fig. 6c). The ideal approach trajectory will give the robot an initial velocity such that the transition maneuver ends close to the apex of the projectile motion, meaning the vehicle has a low vertical velocity. With wings, the acceleration capabilities of the vehicle are reduced due to drag, lowering the projectile motion apex. A larger test space would give the robot more time to accelerate, allowing it to reach a higher apex and enabling recovery. Alternatively, a control approach to the recovery challenge would include enabling higher frequency control and onboard feedback throughout the duration of the transition maneuver so that the orientation can be more precisely controlled during the reverse thrust phase. However, in field applications, recovery into a hover position will not be necessary, and instead the intent would be to recover the vehicle into the target angle of attack and forward velocity. This requires available space in the direction of travel, but should theoretically be easier to achieve because the robot's orientation will not have as much error when compared to a forward flight setpoint.

We observed that snap-through induces a pitch forward motion in the robot, and the rotational dynamics of the vehicle that occur during Q-to-F are not yet fully understood. Two challenging factors are the angular momentum and internal impulsive forces between the two rigid bodies. During snap-through, the robot behaves as two rigid bodies connected by springs, but at each equilibrium, the robot may be approximately treated as one rigid body. One of the bistable arms tends to snap-through before the others and the remainder of snap-through occurs quickly, implying the central platform's angular momentum will be different than that of the ring. The center of the bistable mechanism also has linear momentum relative to

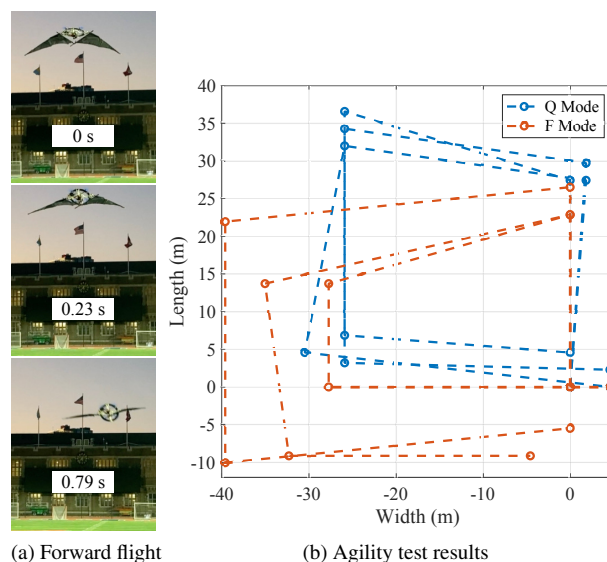


Fig. 7: (a) The BAT in fixed-wing mode flies away from the camera. (b) The agility test boxes are plotted. The pilot is able to fly more accurate boxes when the wings are retracted.

the ring. It is likely that impulsive constraint forces at the pin joints resolve this momentum with that of the resulting system when equilibrium is reached, but since there are multiple pin joints, determining the impulsive forces is challenging. Due to all these factors, the rotational dynamics are difficult to predict precisely, especially given the error in initial angular position and rates due to the open-loop segments. Thus, an important objective for designing a controller following transition would be tolerance to angular perturbations.

6.2 Outdoor Flight Tests

We conducted three types of tests to demonstrate the performance of the aircraft in each flight mode: three hover tests to allow the pilot to gain familiarity of the vehicle, thirteen forward flight tests to verify the stability of the aircraft, and two agility tests to provide a direct comparison between flight modes. Of those tests, one of each type was conducted in quadrotor mode and the remainder were conducted in fixed-wing mode. All outdoor flight testing was conducted over the University of Pennsylvania's football field, Franklin Field. We collected 15.7 minutes of flight time in fixed-wing mode and 9.2 minutes of testing in the quadrotor mode. A table summarizing the outdoor flight tests conducted may be found in [Supplemental Materials Table 3](#).

During all outdoor tests, the robot was flown line-of-sight by a skilled quadrotor pilot standing on the 15-yard line of the football field. Despite never having flown a vehicle equipped with wings previously, the pilot learned how to smoothly transition the robot with wings into forward flight after only two attempts in which the robot did not crash. The pilot is capable of aggressive racing drone flight in rate mode, where angular rate commands are sent to the robot instead of attitude commands. However, we found that attitude mode is sufficient for the steady state flight and beneficial due to the wind and gust disturbances.

We conducted two hover tests in fixed-wing mode and one in quadrotor mode. One hover test flight consists of three 10-second hovers. During the hover test, the pilot destabilized the aircraft by executing agile motions and then stabilized the aircraft and attempted to maintain the position of the aircraft for a period of about 10 seconds.

We conducted twelve forward flight tests in the fixed-wing mode at increasing levels of aggressiveness to demonstrate the stability of the aircraft. We also conducted a forward flight test in the quadrotor mode. In each forward flight test, the pilot started from a hovering position in fixed-wing mode then pitched the aircraft forward while increasing the thrust to enter forward flight. Transitioning into forward flight is known to be challenging for tailsitter VTOL aircraft, but we found that the four rotors give the vehicle sufficient control authority to perform this motion with our non-traditional wing[56]. The wind direction generally aligned with the length of Franklin field, and in each trial the BAT was flown into the wind such that it experienced a headwind. The wind conditions during forward flight tests ranged from 5 mph wind with gusts of 7 mph to 15 mph wind with gusts of 30 mph, as collected by weather data. Transition to forward flight can be seen in Fig. 7a and [Supplemental Materials Video 8](#).

Finally, we conducted agility tests of the robot in both quadrotor and fixed-wing modes ([Supplemental Materials Video 9](#)). Since the null hypothesis was that the pilot's second flight will be at least as good as the first flight if the mode performance is similar, tests were first conducted in quadrotor mode and then in fixed-wing mode to mitigate the effect of increased pilot training time on the results. The pilot was instructed to fly the robot as quickly as possible in a consistent square shape at

Table 1: Agility Test Results

	average		average	
	speed (m/s)	[std]	distance (m)	[std]
Q	6.33	[0.25]	116.3	[4.91]
F	5.13	[0.87]	115.4	[20.7]

a constant altitude over the field. Each agility flight consisted of three agility test trials. In each trial, the pilot started from hover, flew two squares, and then returned to hover. The pilot did not yaw the vehicle, and repeating the squares allowed us to see at least one sharp turn in each direction. We analyzed only the first square of each trial, due to a noticeable sustained gust that caused the pilot to hesitate during one of the second squares. The location of the robot at each corner of the square was extracted using footage from three different camera angles while referencing the yardlines and hashes (Fig. 7b).

6.2.1 Pilot Observations

During the hover test in high wind, the pilot felt that the vehicle was particularly challenging to control in the fixed-wing mode due to the large yawing moments caused by high winds. The BAT tended to align with the wind and the propellers did not yield enough yaw authority to maintain a constant heading. The pilot also noted that while hovering in high winds, the wing started catching air and generating lift already. The additional lift from the wings in moments of high wind required more pilot effort to sustain a constant altitude.

In the forward flight tests, the pilot had a difficult time controlling the aircraft roll, since he had to mentally flip the roll and yaw during flight while pitched forward. The pilot was standing behind the vehicle as it flew down the field, and depth perception of the vehicle was challenging. The vehicle appeared further away than it actually was, sometimes appearing to be near the end zone when it was only at about the 55-yard line.

During the agility tests, the pilot’s anecdotal evidence was that flying agile maneuvers in either mode was more difficult than with a racing drone. This makes sense, since the area reduction of the wings when folded is only 18% in this prototype. The pilot did not qualitatively notice a difference in the maneuverability of the vehicle between the flight modes in the agility tests.

6.2.2 Numerical Data

Processing the high wind hover data shows that the power consumption is consistent with the pilot’s anecdotal evidence that the wings were generating lift. In fact, the pilot supplied lower throttle during the fixed-wing mode hover, and the average power for fixed-wing mode was 434.6 W, compared with 491.9 W in quadrotor mode. This suggests that the wind-tunnel like effect was generating lift, though the robot was remaining stationary.

Contrary to the pilot’s qualitative evidence, the quantitative data from the agility tests suggest that the quadrotor mode is indeed more agile than the fixed-wing mode. Table 1 shows that the pilot operated the quadrotor mode with wings folded about 20% faster (P-value of 0.13 for a t-test on the speeds), and the standard deviations of average speed and distance per square were both about 4 times lower than those of fixed-wing mode ($4.4\times$ and $4.2\times$ lower respectively). Further, the plot of the squares flown in each mode shows that the quadrotor mode allowed for more consistent tracking of the intended flight path (Fig. 7b). This suggests that the pilot needs to compensate less for the effect of the wings when operating in the quadrotor mode, and supports our motivation for the wing folding aircraft.

6.2.3 Discussion

The outdoor flight tests have shown that each flight mode is stable. This also indicates that designing an autopilot for the forward flight mode is feasible as the vehicle is stable enough to fly line-of-sight. In addition, our pilot was able to fly this vehicle with no prior fixed-wing vehicle experience, indicating that expert quadrotor pilots can fly this vehicle with minimal additional training.

The hover and agility tests reveal that folding the wings allows the robot to be more maneuverable. This demonstrates the advantage of this vehicle over hybrid aircraft that cannot change the wing surface area. The difference in agility is expected to be amplified with increasing wing area reduction.

Out of the fifteen flights in the fixed-wing mode, only one hardware failure and three crashes occurred. The hardware failure consisted of one of the wings snapping off due to the high gusts, and the pilot successfully landed the vehicle. The pilot was able to recover the vehicle from many disturbances, including one trial when the robot did a barrel roll due to a large gust. However, the gusts still pose a control challenge and cause crashes. The first of the crashes was at the opposite end of the field, where it is already challenging to perceive the orientation, when the BAT experienced a sudden roll. The pilot tried

to recover the second crash, but the control gains had become saturated due to high winds while in a hovering orientation. For the third crash, the robot was in acro mode, where the pilot directly controls rate commands without stabilization assistance from the PX4 autopilot. With the design of a stabilizing controller for fixed-wing flight, the gusts may be accounted for in some way.

In six of the forward flight trials, snap-through occurred while pitching up and traveling at high speed. The pilot was able to maintain control of the vehicle once it switched to quadrotor mode. Since the vehicle relies on accelerations to trigger the switching, there is an acceleration limit in the fixed wing mode, as well as a critical velocity at which the component of drag force in the direction of folding causes snap-through. It was a design choice to assign the acceleration limit to the fixed wing mode, since for efficient cruising flight the required thrust is generally small. This allows the quadrotor mode to operate without acceleration limits.

In these flight tests, the angle of attack was high (ranging from 30° to 60°). Due to visual perception challenges from the vantage point of the pilot, the vehicle would appear to be pitched forward further than it actually was. Further, tests at optimal angle of attack for this vehicle have yet to be conducted, and the angle of attack varied throughout each flight. The optimal angle of attack for this particular wing is not yet known, but is expected to be similar to that of a flat plate, which has a stall angle of 7-8° angle of attack [57]. At high angles of attack, the robot is operating in a post-stall regime and experiencing a non-optimal amount of drag. The higher than expected angle of attack also means that the effect of gravity on the bistable mechanism will be amplified in our tests. Further, the snap-through of the structure occurred on the testing day with moderate temperature (above 50°F). We observed that the stiffness of the material is greatly increased when the weather is very cold (below 40°F), as occurred on two out of three test days. No snap-through occurred during flights on those days, so the temperature of the environment should be taken into account when the vehicle is deployed.

6.3 Energy Consumption

We conduct a preliminary analysis of the energy consumption in each mode and transition. The power in each mode is computed using the mavros battery status messages reported by PX4 (by multiplying the voltage and current readings). Energy for the transition maneuvers is also computed using the right Riemann summation to numerically integrate the power. The results are shown in Table 2.

First, we compare the data from the indoor test for hovering in each mode. As expected, we find that hover in each flight mode should be similar. However, we are initially surprised that the standard deviation of the quadrotor mode hover power is 6.7 times that of the fixed-wing mode. This is likely due to the wings being taut and out of the prop wash when in fixed-wing mode but hanging loosely below the vehicle and interfering with the prop wash when in quadrotor mode.

A preliminary comparison of the efficiency of each flight mode uses the data from the first side of each box from the agility test. Table 2 shows a comparison of the power for the fixed-wing mode and the quadrotor mode. Comparing the power in each flight mode to the hover in fixed-wing mode suggests that the vehicle already requires 12% less power in forward flight than in hover when in fixed-wing mode, but requires 3% more power in forward flight than in hover when in quadrotor mode.

The transition maneuvers have a higher energy cost than hover due to the high thrusts necessary for snap-through. The data shows that executing the maneuver is energetically equivalent to 2.0 seconds of hover. While this is an initial energy cost to that the robot incurs prior to starting its fixed-wing flight, we find that the break-even point with this modest power decrease is 20 seconds by solving the following relationship for t :

$$P_Q t = E_{QtoF} + P_F t + E_{FtoQ}$$

where $P_Q = 566$ W is the power to fly in quadrotor mode, $E_{QtoF} = 1450$ J is the energy needed for the Q-to-F transition, $P_F = 483$ W is the power to fly in fixed-wing mode, and $E_{FtoQ} = 173$ J is the energy needed for the F-to-Q transition.

These results show progress toward the goal of efficient flight, and that the transition maneuver's energy cost would be recovered after 20 s of flight in fixed-wing mode. However, a t-test shows that the difference in means is not statistically significant ($P=0.09$), and the efficiency of the fixed-wing mode is yet to be fully realized. We have only flown at high angles of attack, so the vehicle was operating in a post stall regime for the wing in these tests. Optimal angle of attack and speed will allow for more efficient motion. These results are also preliminary as we lacked precise robot position measurements. A GPS should be integrated for future tests.

7 Conclusion

We have shown that mid-flight passive dynamic reconfiguration of a bistable structure on an aerial robot is possible. The Bistable Aerial Transformer (BAT) robot uses a combination of compliant mechanism design and specific transition trajectories to transition between two different flight modes. We have shown that the incorporation of the bistable mechanism

Table 2: Energy Consumption of the BAT

	Power (W)	[std]	Energy (J)	[std]
Hover F	551	[5.9]	-	
Hover Q	571	[40.]	-	
F-to-Q	823	[160]	173	[37]
Q-to-F	1170	[60.]	938	[48]
Q-to-F w/approach	1150	[47]	1450	[110]
Forward F	483	[54]	-	
Forward Q	566	[36]	-	

enables the rejection of disturbance forces in addition to the passive mode-switching. Our simulations indicate that hysteresis poses a challenge to the switching system, but that using bidirectional motor directions allows the robot to compensate. Finally, we have shown that the aircraft is stable in each flight mode, and our preliminary analysis suggests that there are agility and efficiency trade-offs between each mode.

Future work includes stabilizing the robot in the fixed-wing mode following the transition. To account for the pitching motion caused by the snap-through, the development of a recovery maneuver is necessary. The results of the wingless tests suggest that it is possible to recover the robot via flipping, but we anticipate that more sophisticated control methods during the reverse thrust segment may be necessary.

The outer ring and the central housing have not been optimized for weight or aerodynamic properties. [Supplemental Materials Table 1](#) shows that the wings and TPU arms are light compared to these frames. The central housing can be redesigned to use minimal material and refabricated from 1/16" carbon fiber. Redesigning the ring to be lighter and less wide will reduce the system weight, boost the prop efficiency, and reduce drag in forward flight. If there is less overlap between the propellers and the frame, there will be more effective area, yielding greater efficiency. Greater efficiency and lower weight will lead to better flight times. Further, the hysteresis of the TPU gives undesired loss of elastic energy, so switching to a spring steel material could help. Using the intuition and data gained through these experiments will aid the development of a mechanism with a similar force displacement curve without substantial hysteresis.

To further quantify the efficiency gains and stability of the aircraft, it is necessary to conduct additional characterization of the wing to determine the optimal angle of attack, as well as the achievable trim speeds and flight path angles. Following characterization of the wing, a fixed-wing flight controller should be developed. Experiments with controlled wind disturbances should be used to characterize the performance of each flight mode of the vehicle in various conditions. and used to conduct real-world experiments with disturbances from gusts. Finally, further investigation into the design of a deployable wing is necessary, since area reduction of the wing is still low with this prototype. Additionally, a wing with greater rigidity will have better lift characteristics than the wing presented. Ideally, a telescoping mechanism can be used to deploy an airfoil shaped wing. This is a challenging design problem on its own, but is important for fully realizing the efficiency gains of this system.

Acknowledgment

We thank Dinesh Thakur and the Kumar lab for sharing their equipment, expertise, control code, and lab space. We would also like to thank Jason Friedman for CAD assistance, Yifan Yuan for 3D printing the TPU arms, Terry Kientz and Jeremy Wang for their assistance with fabricating the HAV frame, Aarushi Singh for help with flight tests, and Erica Feehery, Sarah Ho, Terence Lin, and Razaq Aribidesi for help with the folding wing. We thank Keith Maurer, Dan Gonzalez, Michael Mantz, and Lauren Gerlin for permitting us to conduct testing on Franklin Field.

Funding Data

Support for this project has been provided in part by NSF Grant No. 1943199, 1813624, 2023780, and DGE-1845298, by the Pennsylvania Space Grant Consortium, and by the Penn Center for Undergraduate Research and Fellowships.

References

- [1] Kim, J., Kim, S., Ju, C., and Son, H. I., 2019. “Unmanned aerial vehicles in agriculture: A review of perspective of platform, control, and applications”. *Ieee Access*, **7**, pp. 105100–105115.
- [2] Sun, J., Guan, Q., Liu, Y., and Leng, J., 2016. “Morphing aircraft based on smart materials and structures: A state-of-the-art review”. *Journal of Intelligent material systems and structures*, **27**(17), pp. 2289–2312.
- [3] Zhu, J., Yang, J., Zhang, W., Gu, X., and Zhou, H., 2023. “Design and applications of morphing aircraft and their structures”. *Frontiers of Mechanical Engineering*, **18**(3), p. 34.
- [4] Floreano, D., Mintchev, S., and Shintake, J., 2017. “Foldable drones: from biology to technology”. In *Bioinspiration, Biomimetics, and Bioreplication 2017*, Vol. 10162, International Society for Optics and Photonics, p. 1016203.
- [5] Li, D., Zhao, S., Da Ronch, A., Xiang, J., Drofelnik, J., Li, Y., Zhang, L., Wu, Y., Kintscher, M., Monner, H. P., et al., 2018. “A review of modelling and analysis of morphing wings”. *Progress in Aerospace Sciences*, **100**, pp. 46–62.
- [6] Falanga, D., Kleber, K., Mintchev, S., Floreano, D., and Scaramuzza, D., 2018. “The foldable drone: A morphing quadrotor that can squeeze and fly”. *IEEE Robotics and Automation Letters*, **4**(2), pp. 209–216.
- [7] Zhao, M., Okada, K., and Inaba, M., 2023. “Versatile articulated aerial robot dragon: Aerial manipulation and grasping by vectorable thrust control”. *The International Journal of Robotics Research*, **42**(4-5), pp. 214–248.
- [8] Gerber, M. J., and Tsao, T.-C., 2018. “Twisting and tilting rotors for high-efficiency, thrust-vectorized quadrotors”. *ASME Journal of Mechanisms and Robotics*, **10**(6), p. 061013.
- [9] Baskin, M., and Leblebicioğlu, K., 2023. “Robust attitude controller design for an uncommon quadrotor with big and small tilt rotors”. *ASME Journal of Mechanisms and Robotics*, **15**(3), p. 031003.
- [10] Zhang, X., Kang, X., and Li, B., 2023. “Origami-Inspired Design of a Single-Degree-of-Freedom Reconfigurable Wing With Lockable Mechanisms”. *ASME Journal of Mechanisms and Robotics*, **16**(7), 10, p. 071008.
- [11] Morton, S., and Papanikolopoulos, N., 2017. “A small hybrid ground-air vehicle concept”. In *2017 IEEE/RSJ International Conference on Intelligent Robots and Systems (IROS)*, IEEE, pp. 5149–5154.
- [12] Zufferey, R., Ancel, A. O., Raposo, C., Armanini, S. F., Farinha, A., Siddall, R., Berasaluce, I., Zhu, H., and Kovac, M., 2019. “Sailmav: design and implementation of a novel multi-modal flying sailing robot”. *IEEE Robotics and Automation Letters*, **4**(3), pp. 2894–2901.
- [13] Tan, Y. H., and Chen, B. M., 2020. “A morphable aerial-aquatic quadrotor with coupled symmetric thrust vectoring”. In *2020 IEEE International Conference on Robotics and Automation (ICRA)*, IEEE, pp. 2223–2229.
- [14] Ajaj, R. M., Parancheerivilakkathil, M. S., Amoozgar, M., Friswell, M. I., and Cantwell, W. J., 2021. “Recent developments in the aeroelasticity of morphing aircraft”. *Progress in Aerospace Sciences*, **120**, p. 100682.
- [15] Pham, N. K., and Peraza Hernandez, E. A., 2021. “Modeling and design exploration of a tensegrity-based twisting wing”. *ASME Journal of Mechanisms and Robotics*, **13**(3), p. 031019.
- [16] Ang, K. Z., Cui, J., Pang, T., Li, K., Wang, K., Ke, Y., and Chen, B. M., 2014. “Development of an unmanned tail-sitter with reconfigurable wings: U-lion”. In *11th IEEE International Conference on Control & Automation (ICCA)*, IEEE, pp. 750–755.
- [17] Vourtsis, C., Rochel, V. C., Müller, N. S., Stewart, W., and Floreano, D., 2023. “Wind defiant morphing drones”. *Advanced Intelligent Systems*, **5**(3), p. 2200297.
- [18] Jeong, J., Yoon, S., Kim, S.-K., and Suk, J., 2015. “Dynamic modeling and analysis of a single tilt-wing unmanned aerial vehicle”. In *AIAA Modeling and Simulation Technologies Conference*, p. 1804.
- [19] Sufiyan, D., Win, L. S. T., Win, S. K. H., Pheh, Y. H., Soh, G. S., and Foong, S., 2023. “An efficient multimodal nature-inspired unmanned aerial vehicle capable of agile maneuvers”. *Advanced Intelligent Systems*, **5**(1), p. 2200242.
- [20] Ajanic, E., Feroskhan, M., Mintchev, S., Noca, F., and Floreano, D., 2020. “Bioinspired wing and tail morphing extends drone flight capabilities”. *Science Robotics*, **5**(47), p. eabc2897.
- [21] Xu, J., Du, T., Foshey, M., Li, B., Zhu, B., Schulz, A., and Matusik, W., 2019. “Learning to fly: computational controller design for hybrid uavs with reinforcement learning”. *ACM Transactions on Graphics (TOG)*, **38**(4), pp. 1–12.
- [22] Rus, D., and Tolley, M. T., 2015. “Design, fabrication and control of soft robots”. *Nature*, **521**(7553), pp. 467–475.
- [23] Odhner, L. U., Jentoft, L. P., Claffee, M. R., Corson, N., Tenzer, Y., Ma, R. R., Buehler, M., Kohout, R., Howe, R. D., and Dollar, A. M., 2014. “A compliant, underactuated hand for robust manipulation”. *The International Journal of Robotics Research*, **33**(5), pp. 736–752.
- [24] Yin, A., Lin, H.-C., Thelen, J., Mahner, B., and Ranzani, T., 2019. “Combining locomotion and grasping functionalities in soft robots”. *Advanced Intelligent Systems*, **1**(8), p. 1900089.
- [25] Zhu, J., Lyu, L., Xu, Y., Liang, H., Zhang, X., Ding, H., and Wu, Z., 2021. “Intelligent soft surgical robots for next-generation minimally invasive surgery”. *Advanced Intelligent Systems*, **3**(5), p. 2100011.
- [26] Goncalves, A., Kuppuswamy, N., Beaulieu, A., Uttamchandani, A., Tsui, K. M., and Alspach, A., 2022. “Punyo-1: Soft tactile-sensing upper-body robot for large object manipulation and physical human interaction”. In *2022 IEEE 5th International Conference on Soft Robotics (RoboSoft)*, IEEE, pp. 844–851.
- [27] Bucki, N., and Mueller, M. W., 2019. “Design and control of a passively morphing quadcopter”. In *2019 International Conference on Robotics and Automation (ICRA)*, IEEE, pp. 9116–9122.

- [28] Jia, H., Bai, S., and Chirarattananon, P., 2023. "Aerial manipulation via modular quadrotors with passively foldable airframes". *IEEE/ASME Transactions on Mechatronics*.
- [29] Tang, J., Jain, K. P., and Mueller, M. W., 2022. "Quartm: A quadcopter with unactuated rotor tilting mechanism capable of faster, more agile, and more efficient flight". *Frontiers in Robotics and AI*, **9**, p. 287.
- [30] Bai, S., Ding, R., and Chirarattananon, P., 2022. "A micro aircraft with passive variable-sweep wings". *IEEE Robotics and Automation Letters*, **7**(2), pp. 4016–4023.
- [31] Sun, Y., Wang, J., and Sung, C., 2022. "Repeated jumping with the REBOund: Self-righting jumping robot leveraging bistable origami-inspired design". In *IEEE International Conference on Robotics and Automation (ICRA)*.
- [32] Misu, K., Yoshii, A., and Mochiyama, H., 2018. "A compact wheeled robot that can jump while rolling". In *2018 IEEE/RSJ International Conference on Intelligent Robots and Systems (IROS)*, IEEE, pp. 7507–7512.
- [33] Kim, S., Gribovskaya, E., and Billard, A., 2010. "Learning motion dynamics to catch a moving object". In *2010 10th IEEE-RAS International Conference on Humanoid Robots*, IEEE, pp. 106–111.
- [34] Pal, A., Goswami, D., and Martinez, R. V., 2020. "Elastic energy storage enables rapid and programmable actuation in soft machines". *Advanced Functional Materials*, **30**(1), p. 1906603.
- [35] Chen, T., Bilal, O. R., Shea, K., and Daraio, C., 2018. "Harnessing bistability for directional propulsion of soft, untethered robots". *Proceedings of the National Academy of Sciences*, **115**(22), pp. 5698–5702.
- [36] Meng, L., Kang, R., Gan, D., Chen, G., Chen, L., Branson, D. T., and Dai, J. S., 2020. "A mechanically intelligent crawling robot driven by shape memory alloy and compliant bistable mechanism". *ASME Journal of Mechanisms and Robotics*, **12**(6), p. 061005.
- [37] Thuruthel, T. G., Abidi, S. H., Cianchetti, M., Laschi, C., and Falotico, E., 2020. "A bistable soft gripper with mechanically embedded sensing and actuation for fast grasping". In *2020 29th IEEE International Conference on Robot and Human Interactive Communication (RO-MAN)*, IEEE, pp. 1049–1054.
- [38] McWilliams, J., Yuan, Y., Friedman, J., and Sung, C., 2021. "Push-on push-off: A compliant bistable gripper with mechanical sensing and actuation". In *2021 IEEE 4th International Conference on Soft Robotics (RoboSoft)*, IEEE, pp. 622–629.
- [39] Zhang, H., Sun, J., and Zhao, J., 2019. "Compliant bistable gripper for aerial perching and grasping". In *2019 International Conference on Robotics and Automation (ICRA)*, IEEE, pp. 1248–1253.
- [40] Zheng, P., Xiao, F., Nguyen, P. H., Farinha, A., and Kovac, M., 2023. "Metamorphic aerial robot capable of mid-air shape morphing for rapid perching". *Scientific Reports*, **13**(1), p. 1297.
- [41] Carlson, J., Friedman, J., Kim, C., and Sung, C., 2020. "Rebound: Untethered origami jumping robot with controllable jump height". In *2020 IEEE International Conference on Robotics and Automation (ICRA)*, IEEE, pp. 10089–10095.
- [42] Currier, T. M., Lheron, S., and Modarres-Sadeghi, Y., 2020. "A bio-inspired robotic fish utilizes the snap-through buckling of its spine to generate accelerations of more than 20g". *Bioinspiration & Biomimetics*, **15**(5), p. 055006.
- [43] Nguyen, P. H., Patnaik, K., Mishra, S., Polygerinos, P., and Zhang, W., 2023. "A soft-bodied aerial robot for collision resilience and contact-reactive perching". *Soft Robotics*.
- [44] Ye, K., and Ji, J., 2023. "A novel morphing propeller system inspired by origami-based structure". *ASME Journal of Mechanisms and Robotics*, **15**(1), p. 011006.
- [45] Liu, C., Wohlever, S. J., Ou, M. B., Padir, T., and Felton, S. M., 2021. "Shake and take: Fast transformation of an origami gripper". *IEEE Transactions on Robotics*, **38**(1), pp. 491–506.
- [46] Li, X., McWilliams, J., Li, M., Sung, C., and Jiang, C., 2021. "Soft hybrid aerial vehicle via bistable mechanism". In *2021 IEEE International Conference on Robotics and Automation (ICRA)*, IEEE, pp. 7107–7113.
- [47] Ryseck, P., Jacobellis, G., and Chopra, I., 2021. "Experimental flight testing of wing configurations for high-speed mini quadrotor biplane tail-sitter". *Structure*, **60**, p. 26.
- [48] Li, Y., Li, X., Li, M., Zhu, Y., Zhu, B., and Jiang, C., 2021. "Lagrangian-eulerian multi-density topology optimization with the material point method". *International Journal for Numerical Methods in Engineering*, Mar.
- [49] Chen, Q., Zhang, X., Zhang, H., Zhu, B., and Chen, B., 2019. "Topology optimization of bistable mechanisms with maximized differences between switching forces in forward and backward direction". *Mechanism and Machine Theory*, **139**, Sept., pp. 131–143.
- [50] Bonet, J., and Wood, R. D., 1997. *Nonlinear continuum mechanics for finite element analysis*. Cambridge university press.
- [51] Wang, X., Li, M., Fang, Y., Zhang, X., Gao, M., Tang, M., Kaufman, D. M., and Jiang, C., 2020. "Hierarchical optimization time integration for cfl-rate mpm stepping". *ACM Transactions on Graphics (TOG)*, **39**(3), pp. 1–16.
- [52] Gast, T. F., Schroeder, C., Stomakhin, A., Jiang, C., and Teran, J. M., 2015. "Optimization integrator for large time steps". *IEEE transactions on visualization and computer graphics*, **21**(10), pp. 1103–1115.
- [53] Li, M., Gao, M., Langlois, T., Jiang, C., and Kaufman, D. M., 2019. "Decomposed optimization time integrator for large-step elastodynamics". *ACM Transactions on Graphics (TOG)*, **38**(4), pp. 1–10.
- [54] Li, M., Ferguson, Z., Schneider, T., Langlois, T., Zorin, D., Panozzo, D., Jiang, C., and Kaufman, D. M., 2020. "Incremental potential contact: Intersection- and inversion-free large deformation dynamics". *ACM Transactions on*

[55] Li, X., Li, M., and Jiang, C., 2022. “Energetically consistent inelasticity for optimization time integration”. *ACM Transactions on Graphics*, **41**(4).

[56] Ducard, G. J., and Allenspach, M., 2021. “Review of designs and flight control techniques of hybrid and convertible vtol uavs”. *Aerospace Science and Technology*, **118**, p. 107035.

[57] Amandolese, X., Michelin, S., and Choquel, M., 2013. “Low speed flutter and limit cycle oscillations of a two-degree-of-freedom flat plate in a wind tunnel”. *Journal of Fluids and Structures*, **43**, pp. 244–255.

List of Figures

1	The fabricated BAT prototype with quadrotor (top) and fixed-wing (bottom) modes. Shown hovering during an outdoor flight test over the University of Pennsylvania’s Franklin Field.	2
2	(a) CAD model of the final design. The bistable mechanism (d, shown in blue), is designed via topology optimization and printed from thermoplastic polyurethane. The closeup of the wing linkage (e, boxed in green) also shows an elastic element that is added to counteract the weight of the wing. (b) State transition procedures. *A short forward thrust is used to stabilize the system orientation before the reverse thrust. (c) The control system diagram.	4
3	(a) A photo of the compression testing setup on the MTS machine. (b) The MTS data for the optimized arms of the robot with simulated curves and final arm design overlaid. The simulated curve used in the optimization is shown, along with the calibrated curves with and without hysteresis that match the MTS data. Zero in the displacement corresponds to the location of the axles. Forces and displacements increase in the downward direction (towards quadrotor mode). The plot shows the mean with +/- standard deviation shaded for each tested speed, and the local extrema on each curve are indicated with a point. During flight, the speed is 88 mm/s on average. The test is repeated for slower speeds to determine the effect of the dynamics on the system. Each test includes 5 cycles at each speed, except 0.003 mm/s, which only includes 3 cycles.	6
4	We verify the BAT within our elastodynamic simulation framework. In plots (a) and (c), the displacement refers to the motion of the bistable mechanism, with 40 mm corresponding to fixed-wing mode and -15 mm corresponding to quadrotor mode. (a) The Q-to-F transition is only triggered in the absence of hysteresis. (b) The strain energy plots show that the hysteresis adds dampings to the system. (c) The displacement plot shows that when reverse thrust is used, the transitions are successfully triggered. Per-motor thrust values are also plotted.	10
5	Snapshots from Supplemental Materials Video 6 of the mode transitions. [Top] F-to-Q: The BAT begins in fixed-wing mode and applies a large thrust. Around 0.13 seconds, the bistable mechanism has snapped-through to the other equilibrium, causing the wings to fold. [Bottom] Q-to-F: the BAT begins hovering in quadrotor mode, executes a vertical trajectory, pitches forward to 90°, and reverses the direction of thrust. Snap-through and wing deployment occurs, with a side effect of inducing a forward pitch.	10
6	Experimental Data from the Flight Tests. Top plots show the motion of the bistable mechanism and the control inputs, indicated by shaded regions, middle plots show the predicted, commanded, and actual position of the robot z coordinate during the transitions, and bottom plots show the actual pitch rate and thrust commands sent to the robot during the trials. (a) For F-to-Q, the displacement plot shows snap-through, and the robot z coordinate shows that the robot continues flying after snap-through. (b) For visual clarity, light smoothing is applied to the bistable mechanism displacement for Q-to-F (a moving median filter with a window of width three) due to orientation errors from marker occlusion. With the wings attached, the controller is not able to track the approach trajectory very well due to drag, preventing the robot from reaching the desired apex. (c) For Q-to-F without the wings, the snap-through takes longer. When the wings are not attached the robot tracks the commanded trajectory with a lag. The two trials with shallower end behavior were able to hover after snap-through.	11
7	(a) The BAT in fixed-wing mode flies away from the camera. (b) The agility test boxes are plotted. The pilot is able to fly more accurate boxes when the wings are retracted.	13

List of Tables

1	Agility Test Results	14
2	Energy Consumption of the BAT	16
1	Mass Breakdown of the BAT	21
2	Design parameters for the topology optimization	21
3	Outdoor Flight Test Summary	22

Supplemental Material

Supplemental Section 1: Wing Fabrication

The robot's wing deployment mechanism consists of a four-bar linkage that folds and unfolds a fabric wing surface. The wing linkage design is as discussed in our previous work^[46] (Video S3, Supplementary Materials), and it amplifies and transforms the angular rotation of the bistable mechanism at the pin joints into rotation of the wing. The linkages were laser cut from 1/4" acrylic sheet and connected using 1/8" diameter shoulder screws. The wing linkage is attached to the bistable mechanism via a part 3D printed from PLA.

The wing is formed from a repurposed 48" inversion umbrella spar⁵, consisting of a long link and a short link. This frame is coupled to the wing linkage using strong adhesive tape, such that the long link is parallel to the wing output linkage. Fishing line is used to add tension into the long link of the spar, and polyester fabric is sewn over the spar to create the triangular wing surface. A thin metal rod is bent into a C-shape and sewn into the wing surface to give additional tension to the middle of the wing. In the center of the robot, the spar is connected to the front and back of the central platform with fishing line so that its out-of-plane motion is constrained without being fully fixed (Figure S1, Supporting Information).

Supplemental Section 2: Control System Architecture

The robot's onboard flight controller is a Pixracer mounted to the rigid ring of the robot. The Pixracer runs the PX4 autopilot software onboard, handles the low-level attitude control, monitors the power consumption of the motors, and records flight data to an SD card. The Pixracer is also equipped with inertial measurement units (IMUs) that it uses as feedback to the onboard attitude controller. The Pixracer receives attitude setpoints, which consist of collective thrust as well as the desired orientation quaternion of the robot and/or the desired angular rates (roll, pitch, yaw). To achieve the attitude setpoint, the Pixracer computes and transmits commands for the ESCs connected to the motors. We use a customized version of the PX4 that allows the attitude setpoints to have a negative thrust command. When a negative collective thrust is provided, all motors' directions will reverse.

When PX4 is set to a stabilized flight mode, the vehicle computes the angular rate setpoints onboard given the current and desired orientations. During rate mode, PX4 directly receives the angular rate setpoints and there is no target orientation. Attitude setpoints can either be received from the Spektrum DX6i radio transmitter or received via the ESP8266 wifi module.

For the human piloted outdoor tests, only the Spektrum DX6i radio transmitter is used for flight. It is used to send the commands to arm and disarm the robot at the beginning and end of the flight tests. Joysticks on the transmitter allow the pilot to specify the attitude setpoints that are sent to the Pixracer. For the controlled indoor tests, the transmitter and the wifi module are both necessary for flight. The transmitter has a mode switch to determine whether the Pixracer will receive the attitude setpoints from the transmitter or those from the wifi module. After arming the vehicle and switching to offboard mode, commands sent via the joysticks are ignored by the Pixracer. Instead, attitude setpoints are computed by a high-level controller running on a ground control station (GCS). Then, setpoints are transmitted to the ESP8266 wifi module using the MAVLink communication protocol.

During indoor tests, the GCS is a laptop running ROS. It is connected to both the vehicle and a Vicon motion capture system on separate wifi networks. The Vicon system tracks the ring and the central platform as two separate rigid bodies, but only the ring's odometry is used for control. A trajectory tracker computes desired positions at each time step to drive the robot along a given trajectory. The tracker sends position commands to the high-level SO3-based controller⁶ that takes in state information from the Vicon system and a position command. The controller computes the attitude setpoint for the robot at the current time step and transmits it to the robot using a MAVLink interface. The propeller thrust coefficient is used in the computation of the attitude setpoint (Figure S2).

We use two different trajectory tracking methods to generate position commands for the SO3-based controller. The first tracking method is a minimum jerk line tracking method that takes in a desired final location of the robot, the current position of the robot, and the total time the trajectory should take. At each time step, the line tracker incorporates feedback on the current robot position to compute a position command to send to the controller. This trajectory tracker is used for launching the robot, conducting hover tests, and guiding the robot to the start location of a mode transition. The second tracking method is one that tracks a piece-wise polynomial trajectory in a strictly time-based manner. This tracker is used to track specific trajectories. At each time step, the polynomial tracker sends a position command to the SO3-based controller based only on the current time (relative to the start of the trajectory). The two main differences between the polynomial tracker and the line tracker are: the polynomial tracker allows the specification of multi-segmented polynomials for easy modification of the speed throughout the trajectory, and this polynomial tracker does not depend on the robot's current position, meaning that it will provide the same commands to the robot each time it is executed. Note that there is still position feedback in the SO3-based controller that receives the position commands from both trajectory trackers.

⁵www.geiger.com/p/48-arc-soho-tartan-inversion-umbrella-522011?pid=368594

⁶https://github.com/KumarRobotics/kr_mav_control

Supplemental Figure Caption List

1. Metal rods are placed on each wing to help with rigidity of the fabric material. Fishing line is connected from the bottom of one wing, passed through the fishing line attachment at the back of the battery, and then connected to the bottom of the other wing. This is repeated with a second piece of fishing line that passes through the attachment at the front of the battery. A third piece of fishing line connects the bottom wing tips to each other.
2. Thrust stand test data for the Dalprop T5045C propellers on the ARRISX2206 2450kV motors. The controller used in this paper uses a quadratic relationship between propeller speed (ω) and thrust force (F) via a thrust coefficient k_f , $F = k_f \omega^2$. We determine k_f for the propeller by conducting thrust stand testing. The ESC is ramped from 0 to 2300 rad/s gradually, thrust is measured by a bar load cell, and the angular velocity is measured optically by tracking a piece of white tape on the motor. To compute k_f , we perform linear least squares regression with the quadratic model. For the forward thrust direction $k_{f,f} = 1.06 \times 10^{-6} \text{ N (s/rad)}^2$, while in the reverse thrust direction $k_{f,r} = -5.93 \times 10^{-7} \text{ N (s/rad)}^2$. While only the forward $k_{f,f}$ is supplied to our controller, determining the reverse thrust $k_{f,r}$ shows that the amount of thrust available when spinning the motors in reverse is 56% of the corresponding amount of forward thrust.

Supplemental Tables

Table 1: Mass Breakdown of the BAT

Component	Mass (g)
Battery	183
Ring	167
Propulsion	155
Electronics	94
Central Housing	79
Wings	111
TPU arms	31
Other	7
Total	827

Table 2: Design parameters for the topology optimization

Parameter	Value	Description
u_i^1	10 mm	Peak reaction force location
u_i^2	50 mm	Valley reaction force location
\bar{V}	0.2	Volume Fraction
α	50	Weighting between objectives
E	$5.5 \times 10^6 \text{ Pa}$	Young's Modulus During Optimization
f_1^*	4 N	Peak target force
f_2^*	1.2 N	Valley target force
f	$-f_1^* n$	Force applied to port i at u^3

Table 3: Outdoor Flight Test Summary

Mode	mm-dd-yy[hh]	#Flights	Test Type	Wind [Gusts] (mph) [†]	Temp (°F)	Duration (s)	Crashes
F	12-19-22[14]	2	hover	15 [29]	35	221	0
F	12-19-22[14]	1	forward	15 [29]	35	25	1
F	12-21-22[10]	1	agility	5 [7]	37	194	0
F	12-21-22[10]	3	forward	5 [7]	37	210	2
F	01-18-23[17]	2	forward ^a	12 [21]	50	120	0 ^b
F	01-30-23[17]	6 ^c	forward	6 [8]	54	172	0
Q	12-19-22[14]	1	hover	15 [29]	35	110	0
Q	12-21-22[10]	1	agility	5 [7]	37	170	0
Q	01-30-23[17]	1	forward	6 [8]	54	134	0
Q	01-30-23[17]	6 ^c	recovery	6 [8]	54	140	0
F Total	-	15	-	-		942	3
Q Total	-	9	-	-		554	0
Total	-	18	-	-		1496	3

^a Due to gust severity, the pilot spent one of these trials maintaining stability of the aircraft

^b Due to gusts, one of the wings snapped off, but the pilot successfully landed the aircraft

^c Transition from F to Q occurred at the end of the forward flights, and the aircraft was landed in Q mode. The data from these 6 flights is split into modes

[†]Wind and temperature data is taken from the weather archive for the day of testing and gust information is from <https://phillyfed.alerteagle.com/history90.aspx>.